

# Targeted High-Resolution Structure from Motion Observations over the $M_w$ 6.4 and 7.1 Ruptures of the Ridgecrest Earthquake Sequence

Andrea Donnellan<sup>\*1</sup>, Gregory Lyzenga<sup>1</sup>, Adnan Ansar<sup>1</sup>, Christine Goulet<sup>2</sup>, Jun Wang<sup>3</sup>, and Marlon Pierce<sup>3</sup>

## Abstract

We carried out six targeted structure from motion surveys using small uninhabited aerial systems over the  $M_w$  6.4 and 7.1 ruptures of the Ridgecrest earthquake sequence in the first three months after the events. The surveys cover approximately 500 × 500 m areas just south of Highway 178 with an average ground sample distance of 1.5 cm. The first survey took place five days after the  $M_w$  6.4 foreshock on 9 July 2019. The final survey took place on 27 September 2019. The time between surveys increased over time, with the first five surveys taking place in the first month after the earthquake. Comparison of imagery from before and after the  $M_w$  7.1 earthquake shows variation in slip on the main rupture and a small amount of distributed slip across the scene. Cracks can be observed and mapped in the high-resolution imagery, which show an echelon cracking, fault splays, and a northeast-striking conjugate fault at the  $M_w$  7.1 rupture south of Highway 178 and near the dirt road. Initial postseismic results show little fault afterslip, but possible subsidence in the first 7–10 days after the earthquake, followed by uplift.

**Cite this article as** Donnellan, A., G. Lyzenga, A. Ansar, C. Goulet, J. Wang, and M. Pierce (2020). Targeted High-Resolution Structure from Motion Observations over the  $M_w$  6.4 and 7.1 Ruptures of the Ridgecrest Earthquake Sequence, *Seismol. Res. Lett.* **XX**, 1–9, doi: [10.1785/0220190274](https://doi.org/10.1785/0220190274).

## Introduction (Experiment Motivation)

The Ridgecrest earthquake sequence began on Thursday, 4 July 2019 at 10:33 a.m. local Pacific Daylight time (PDT), following some smaller earthquakes, with an  $M_w$  6.4 northeast-striking left-lateral earthquake northeast of the town of Ridgecrest and south of China Lake. The event was followed by an aftershock sequence, an  $M_w$  5.4 event at 04:08 a.m. PDT on 5 July 2019, and the  $M_w$  7.1 mainshock at 08:19 p.m. PDT on 5 July 2019. The  $M_w$  7.1 event initiated north of the northeast end of the  $M_w$  6.4 earthquake and ruptured bilaterally. The  $M_w$  6.4 and 7.1 events ruptured the ground surface. The majority of both ruptures occurred within the Naval Air Weapons Station (NAWS) China Lake and were not easily accessible. The southern portions of both earthquakes ruptured south of China Lake, which is bounded to the south by Highway 178.

To observe any postseismic afterslip on the ruptures, we targeted small areas of both ruptures using small uninhabited aerial systems (sUAS) or drones. We selected our survey areas based on detailed field mapping conducted immediately following the earthquake sequence (Brandenberg *et al.*, 2019; C. A. Goulet *et al.* unpublished manuscript, 2020, see [Data and Resources](#)). Locations were just south of Highway 178 on the  $M_w$  6.4 and 7.1 ruptures (Fig. 1). Both were easy to access, as close to the epicenters as possible, given the restricted

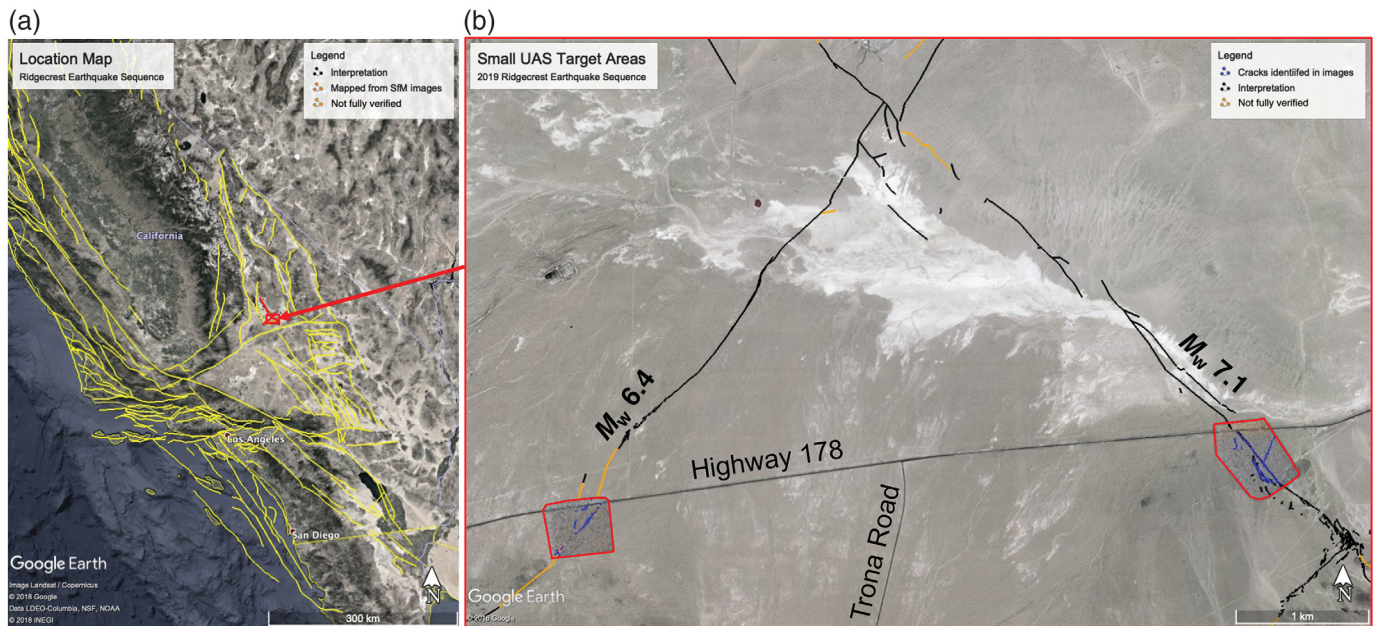
Naval Air Weapons Station China Lake and exhibited clear surface ruptures.

The goal of the observations was to collect repeated structure from motion (SfM) observations at targeted areas of each rupture to measure postseismic motion over time. Because the ruptures were fairly long and continuous, in relatively consistent geologic structure, we assumed that relative small area measurements within the ruptures would reflect similar behavior of the fault along much of the length of the rupture. The rupture length for the  $M_w$  6.4 rupture is on the order of 15 km, and the rupture of the  $M_w$  7.1 is on the order of 50 km, whereas the length of fault sections measured by our surveys is on the order of 0.5 km. Our focus was on understanding temporal evolution of the fault zone at small targeted locations. The goal was to compare afterslip for this earthquake to afterslip observed for the 1992  $M_w$  7.3 Landers earthquake sequence (Hauksson *et al.*, 1993) and 1999 Hector Mine earthquake (Dreger and Kaverina, 2000) that also occurred in the Eastern

1. Jet Propulsion Laboratory, California Institute of Technology, Pasadena, California, U.S.A.; 2. Southern California Earthquake Center, University of Southern California, Los Angeles, California, U.S.A.; 3. Indiana University, Cyber Infrastructure Building, Bloomington, Indiana, U.S.A.

\*Corresponding author: [andrea@jpl.caltech.edu](mailto:andrea@jpl.caltech.edu)

© Seismological Society of America



California Shear Zone. The Landers earthquake showed shallow fault afterslip in the centimeter range (Sylvester, 1993; Shen *et al.*, 1994) and the Hector Mine earthquake experienced decimeters of slip at survey mode Global Positioning System (GPS) stations (Jacobs *et al.*, 2002; Owen *et al.*, 2002). These measurements can be used combined with Global Navigation Satellite System and Interferometric Synthetic Aperture Radar (InSAR) measurements to test whether afterslip extends to the surface or occurs deeper in the crust. Shallow slip would show up in the repeated local surveys and possibly in the other geodetic surveys, whereas deeper slip only would not be detectable within the local survey areas but might be with the broader coverage methods.

The areas surveyed were also to cover a wide enough zone across each rupture to measure shallow off-fault deformation. Coseismic off-fault deformation can be assessed from the width of the observed fracture zone and different fault strands in the local area. High-resolution observations that span a sufficient width across the fault zone can also be compared to determine the amount and extent of distributed deformation within the survey area. Identification of fractures and surface rupture can be compared to those identified from field mapping or other methods.

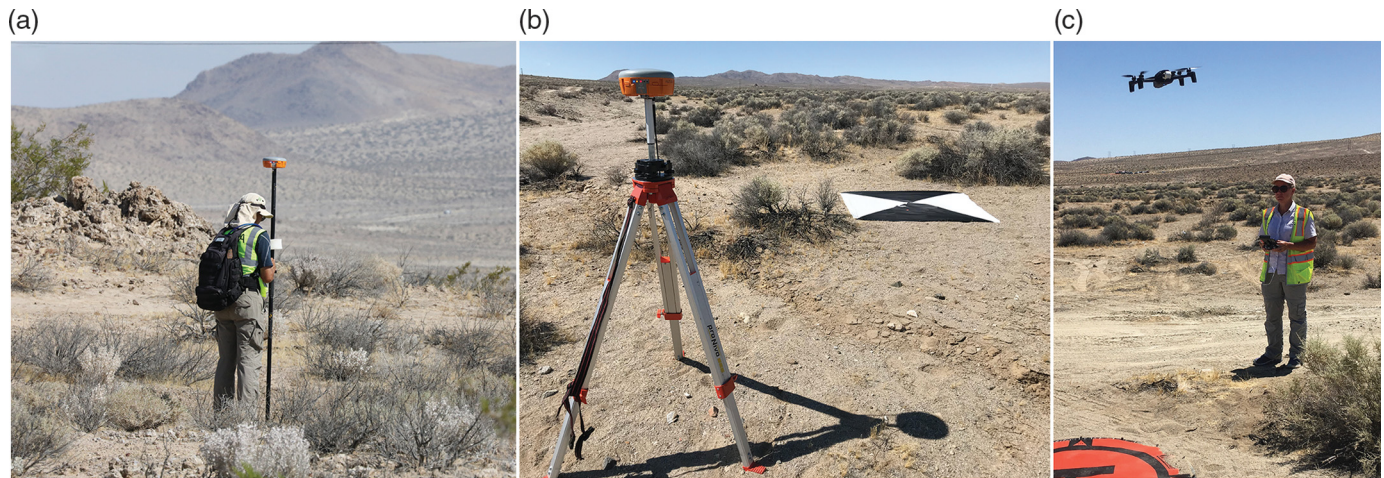
## Instrument Deployment and Details

We carried out repeated measurements over the  $M_w$  6.4 and 7.1 ruptures south of Highway 178 (Table 1; Fig. 1). Data were collected using Parrot Anafi sUAS (Fig. 2). The vehicles each have a 21 megapixel integrated camera and gimbal and an onboard standard accuracy GPS, which geotags the images. We flew our surveys using an app called Pix4DCapture, a free flight planning app for mobile devices from Pix4D (see [Data and Resources](#)). We flew double grids with the camera facing forward, 20° up from nadir. The images had a front overlap of 80° and a side overlap of 70°. We flew the vehicles at 45 m above ground level, balancing coverage, flight time, and ground sample distance.

**Figure 1.** (a) Location map of Ridgecrest rupture sequence. Yellow lines show Uniform California Earthquake Rupture Forecast, Version 3 (UCERF3) (Field *et al.*, 2015) faults for context. Red lines show rupture locations. Red arrow points from study location. (b)  $M_w$  6.4 and 7.1 ruptures near Highway 178. Black lines show interpreted ruptures (Scharer, written comm., 2019). Red boxes outline structure from motion (SfM) target areas and orthomosaic results. Orange lines show not fully verified ruptures, and blue lines show cracks inferred from the SfM products.

Pix4DCapture saves the projects, so we were able to reproduce the flights for each survey. We made minor adjustments to the surveys between the early flights.

We deployed cloth iron cross survey targets, which we have left at the study locations (Fig. 2). As of our last survey for this article, all of the targets were still in place. Because the targets serve as reference points within each survey in time, it does not matter if they move between surveys. We added one more target to the  $M_w$  6.4 rupture to improve the geometry after the second survey and also slightly expanded our flight survey grid. By late September, we had staked down the center of each ground control point (GCP) with the goal of preserving their locations and presence. As discussed subsequently, locations of the targets moved up to 10 cm between surveys and are probably not useful for determining any postseismic motions within the survey area. We surveyed the GCPs using a Septentrio Real Time Kinematic (RTK) GPS system with base and rover stations. We logged data at the base station while we flew and post processed the data using the National Geodetic Survey's mail in Online Positioning User Service (OPUS) processing system. The base station broadcasts RTK corrections to the rover, and the location of the rover relative to the base station was recorded for each GCP. The formal error for the base station solutions produced by OPUS is 1.1–1.7 cm. We corrected the location



of the GCPs after we obtained the OPUS solution using software we wrote at Jet Propulsion Laboratory (JPL) called OpusCorrect.py. The root mean square (rms) error of the GCPs, based on Pix4d output, is about 2 cm. We reserved one target as a check point to validate the precision.

We collected six sets of observations at each location with the time between observations increasing as time since the earthquakes increases (Table 1). Postseismic motions typically follow a log decay (Scholz, 1972), which is the rationale for increasing time between observations as time passes. We will continue to collect data infrequently over time.

We downloaded the images from the vehicles and processed them using the commercial software package Pix4Dmapper, which is designed to produce survey grade results (see Data and Resources). Pix4D is a commercial photogrammetry software package tailored to sUAS. The software generates 3D reconstructions using a technique called SfM in which shape is determined from images collected from different perspectives (Wallach and O'Connell, 1953; Ullman, 1979; Marr, 1980). The initial step is to load geotagged images of the survey area into Pix4D and run an initial solution in which keypoints in the

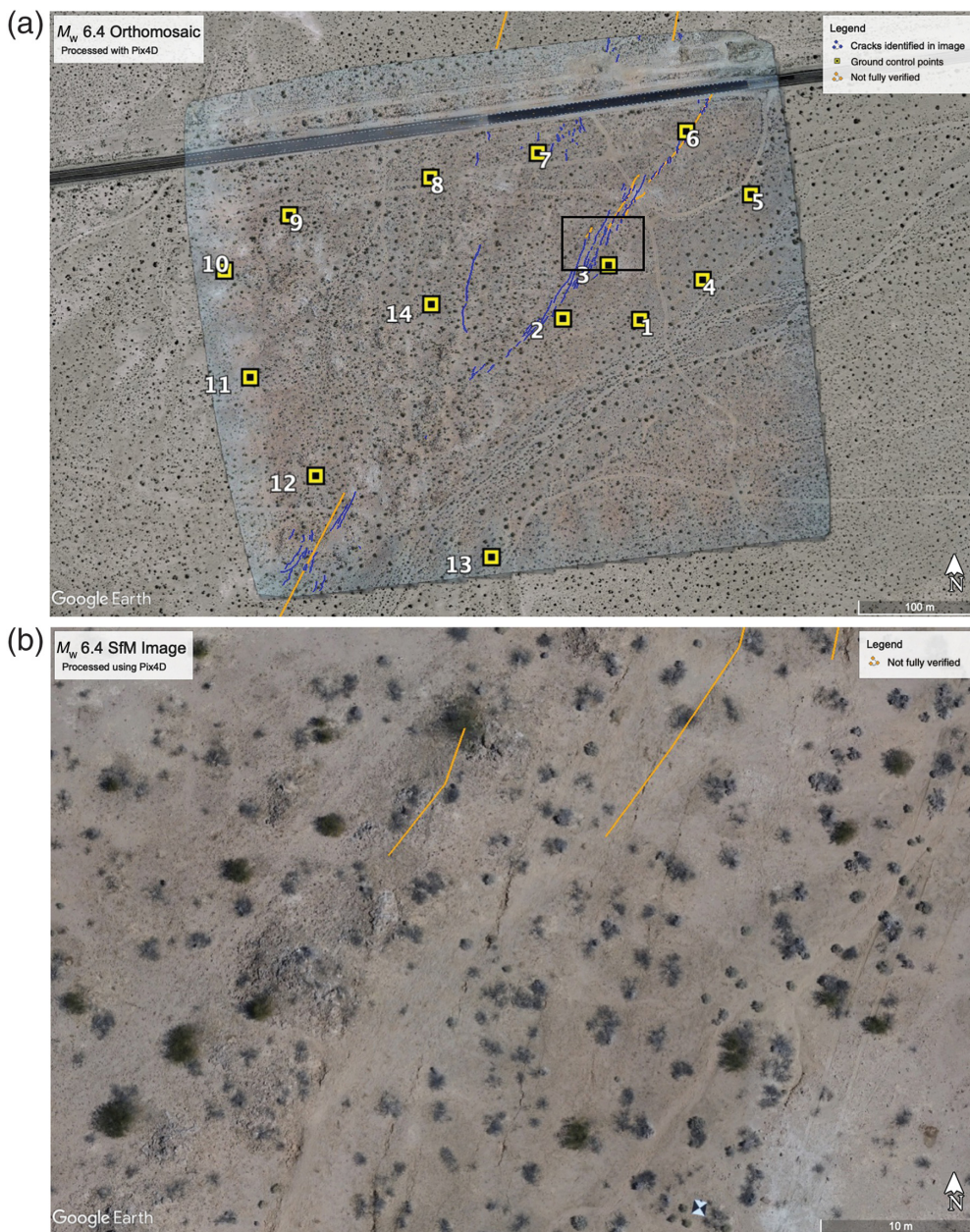
**Figure 2.** (a) Typical field observations include observing a ground control point (GCP) with a rover Global Positioning System (GPS) antenna on a 2 m pole, (b) a base station broadcasting Real Time Kinematic (RTK) GPS corrections with iron cross ground control targets to be surveyed with the rover, and (c) a small uninhabited aerial systems (sUAS) flying an autonomous flight plan, but controlled by a pilot.

image are identified. After this step the locations of the GCP targets are loaded, found in multiple images, and registered to their precise location, which constrains the geometry and improves accuracy of the overall solution. The next step is to re-estimate the camera model and solution, followed by generation of a point cloud, digital surface model, and orthomosaic. The precise products are orthorectified and geocoded. Products include point clouds at native resolution, 2 cm gridded digital surface models, orthomosaics, Keyhole Markup Language (KML) output of the images, files of GCPs corrected into a precise solution, and a quality report for each set of observations. The results are posted to GeoGateway (see Data and Resources) under the 3D imaging tab (Donnellan *et al.*, 2019).

TABLE 1  
**Dates, Times, and Number of Images Collected for Each Location**

Date (yyyy/mm/dd)	$M_w$ 6.4				$M_w$ 7.1			
	Time (PDT)	Number of Images	Average GSD	Area Covered	Time (PDT)	Number of Images	Average GSD	Area Covered
2019/07/09	10:09–11:30	1,243	1.55 cm	0.194 km <sup>2</sup>	13:30–16:22	439	1.63 cm	0.149 km <sup>2</sup>
2019/07/11	13:28–15:28	1,220	1.55 cm	0.193 km <sup>2</sup>	12:08–12:48	2,049	1.68 cm	0.275 km <sup>2</sup>
2019/07/15	09:19–10:29	1,301	1.50 cm	0.198 km <sup>2</sup>	11:08–13:24	1,755	1.70 cm	0.268 km <sup>2</sup>
2019/07/22	10:08–11:45	1,302	1.53 cm	0.198 km <sup>2</sup>	12:21–14:22	1,525	1.70 cm	0.275 km <sup>2</sup>
2019/08/08	09:33–10:51	1,194	1.48 cm	0.199 km <sup>2</sup>	11:24–14:12	1,923	1.64 cm	0.277 km <sup>2</sup>
2019/09/27	07:59–10:01	1,100	1.40 cm	0.189 km <sup>2</sup>	10:38–12:47	1,774	1.56 cm	0.266 km <sup>2</sup>

Time span is the rough time of image collection based on Global Positioning System (GPS) measurements and gives rough indication of sun angle. GSD, ground sample distance.



**Figure 3.** (a) Orthomosaic of the  $M_w$  6.4 rupture shown on Google Earth image, with traced surface cracks in blue. Orange lines represent not fully verified trace from the U.S. Geological Survey (USGS) (Pickering *et al.*, 2019; Ponti *et al.*, 2020). Ground control points, shown as yellow boxes, are labeled. (b) Expanded area marked as a box in (a). Identified surface cracks are not marked to show the surface cracking. The USGS rupture lines, which are not fully verified for this location, are shown.

### Overall Data Quality and Availability

The data products are generally consistent. Severe heat caused some degradation of the camera sensor resulting in some vignetting apparent in the orthomosaic, which produces some faint striping in a grid pattern. The Parrot Anafi would occasionally stop recording data, despite providing feedback to the operator that the camera was functioning normally. This resulted in loss of data on the first day on 9 July 2019 at the  $M_w$  7.1 rupture.

Flight duration on a single battery is typically about 20 min. Three 20 min flights cover the flight area at the  $M_w$  6.4 rupture and five flights are required at the  $M_w$  7.1 rupture. In subsequent flights, after our first day of observations, we downloaded data between each flight to check that the data had been written to the micro SD card. Days showing longer durations at a location are due to troubleshooting and conducting reflights to obtain the desired data.

In general, the days were fairly cloud free, and, except for the 11 July 2019, measurements occurred at roughly the same time of day. A few shaded areas can be seen in some of the orthomosaics from clouds obscuring the sun. Color tone changes in the overall product are typically due to the presence of a cloud. In general, we have flown the  $M_w$  6.4 rupture in the morning and the  $M_w$  7.1 rupture in the afternoon. This order was switched on 11 July 2019, resulting in different shadowing on the two products from that day. However, the shadowing at the 11 July 2019  $M_w$  7.1 rupture made it easier to find surface cracking in the image product.

### Initial Observations

We used the 9 July 2019  $M_w$  6.4 and the 11 July  $M_w$  7.1 KML files to trace surface cracks from the earthquakes (Figs. 3 and 4). We

chose these two days because the lighting was the best, and the products were complete on these days for the respective locations. We plotted our surface crack identifications with the KML file provided by Kate Scharer of the U.S. Geological Survey (USGS) field mapped and verified and not fully verified rupture traces (Pickering *et al.*, 2019; Ponti *et al.*, 2020). In general, our results are complementary to the USGS results. Our traces overlap the USGS traces. There

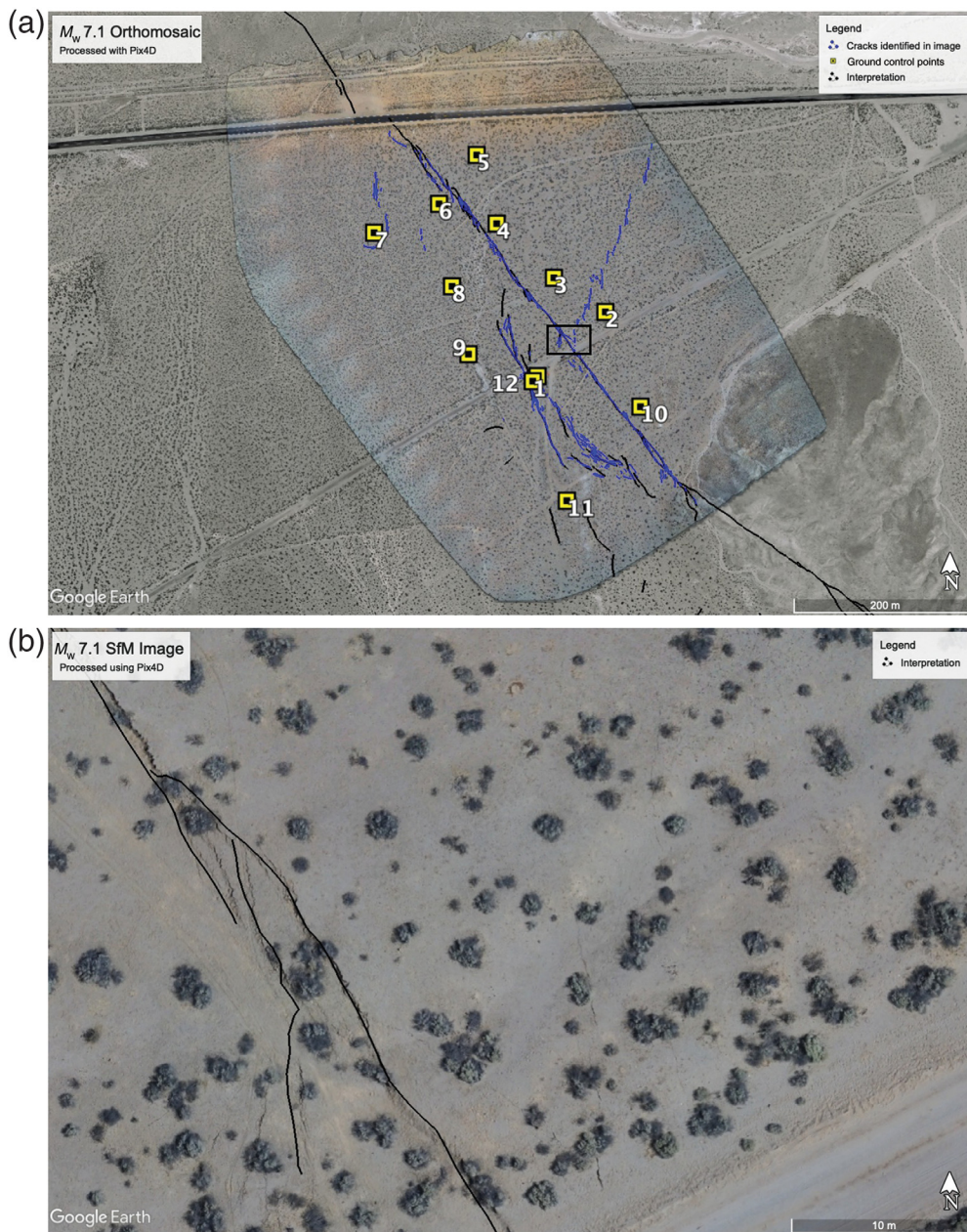


**Figure 4.** (a) Orthomosaic shown on Google Earth with USGS rupture traces shown in black (Pickering *et al.*, 2019; Ponti *et al.*, 2020), and identified surface cracks from the orthomosaic shown in blue. Ground control points are labeled. (b) Expanded area marked as a box in (a) shows surface cracking and traces mapped by the USGS (Pickering *et al.*, 2019; Ponti *et al.*, 2020).

are gaps in the USGS measurements, which are filled in by our surface crack locations.

## Initial Results

Surface cracking identified in the sUAS imagery shows a series of en echelon cracks in a lineation, striking northeast, for the  $M_w$  6.4 earthquake (Fig. 3). Two splays from the northeast part of the image join together in the center of the image. Where these two splays join, there is a gap in surface cracking about

100 m long. Surface cracking then continues to the southwest corner of the image.

The  $M_w$  7.1 earthquake ruptured as a right-lateral normal fault, which can be mapped along the length of the sUAS image (Fig. 4). The fault offsets are west at the road to the north. Subparallel to and east of the main rupture is a series of cracks that are less continuous and less aligned that form the western boundary of a small graben between those cracks and the main rupture. In the center of the image, a series of en echelon cracks from a northeast-striking lineation, suggesting that some conjugate faulting occurred near this part of the  $M_w$  7.1 rupture. It should be noted that surface cracks were identified with the image zoomed in to cover about a  $20 \times 20$  m area. Only after the cracks were identified was it clear that they formed a northeast-striking lineation.

The right-lateral motion and larger cracking is easily seen when toggling between a before Google Earth image and our after image. A KML of our image can be downloaded from the 3D Imaging tab (see [Data and Resources](#)). Using the Google Earth image, which appears to be a 30 cm image obtained from Digital Globe and collected on 1 July 2017, we carried out subpixel horizontal change detection between the two images (Fig. 5). Future analysis will be using a Digital Globe image, when we complete the licensing and acquire the image from National Aeronautics and Space Administration (NASA) Goddard Space Flight Center. The results show localization of fault slip to the southeast along the rupture with the more distributed deformation on the western side. This may be due in part to the westward stepover of the rupture near the north of the image at Highway 178.

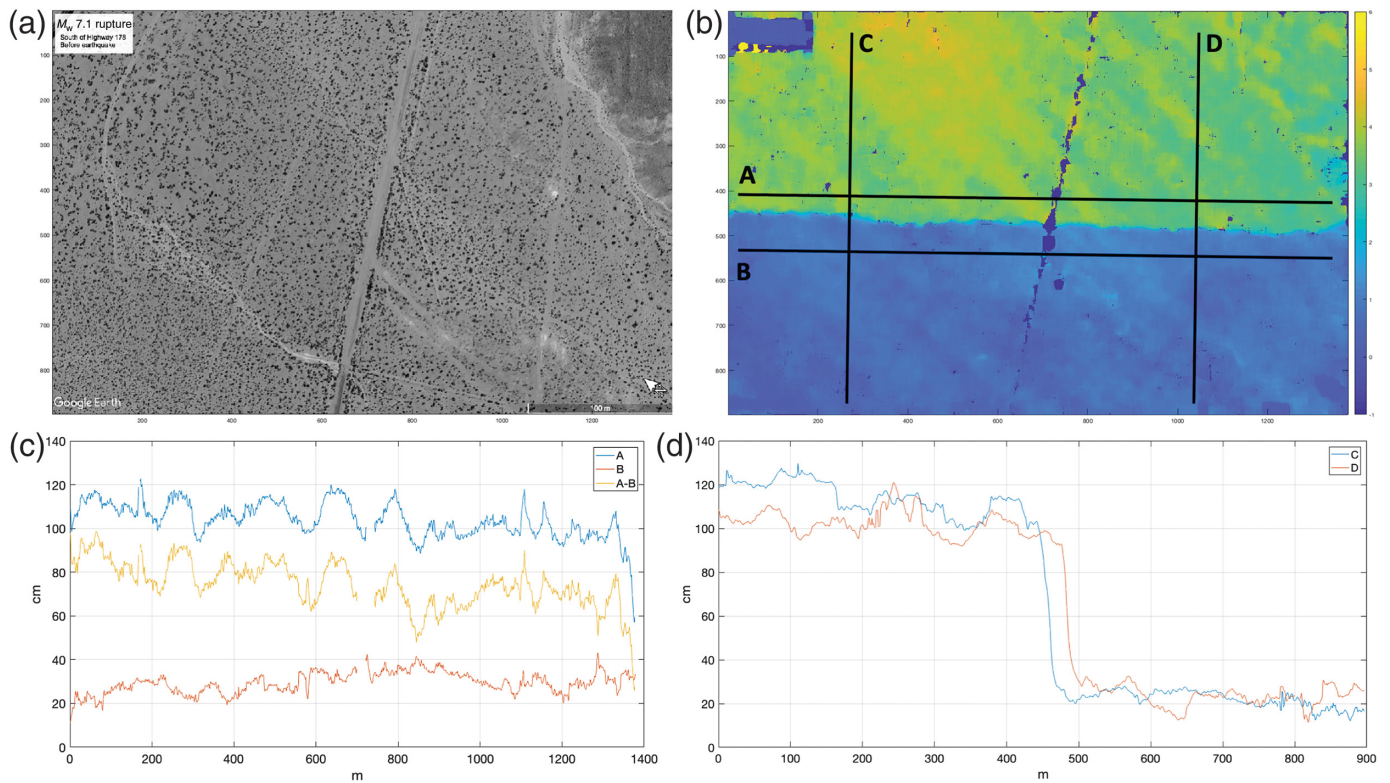


**Figure 5.** (a) Reference image of the  $M_w$  7.1 rupture showing the area used for change detection. Image is rotated so that the fault rupture is horizontal in the image. (b) Change image using an image from Google Earth as the before image and the image collected on 9 July 2019 with the sUAS as the after image. Blue color shows left motion, and yellow color denotes rightward

motion. Blue color in top left is an artifact from the image legend. (c) Change along the fault on profiles A and B and the difference between the two profiles from left to right or northwest to southeast in the image. (d) Change along profiles C and D across the fault from top to bottom, or east to west in the image.

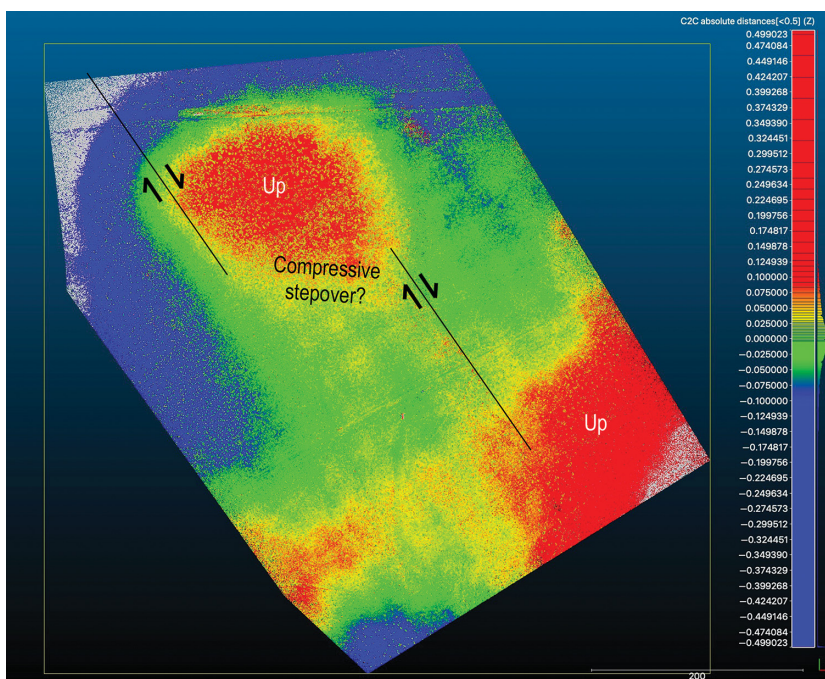


**Figure 6.** Vertical change between images collected during 15 July 2019 and 11 July 2019 for the  $M_w$  7.1 rupture.

We used the open-source Cloud Compare to carry out change detection of pairs of images following the earthquake. There is very little post-seismic deformation. Some vertical change is detectable for the  $M_w$  7.1 rupture (Fig. 6). Uplift may occur near the step-over toward the north in the image. Uplift, where there are mine tailings, also occurs at the southern end of the image. The main rupture exhibited normal slip from the mainshock with the east side up. Point cloud comparisons suggest that this same area subsided with east side down following the earthquake. Later surveys suggest possible centimeter level north, west, and upward motion of the scene.

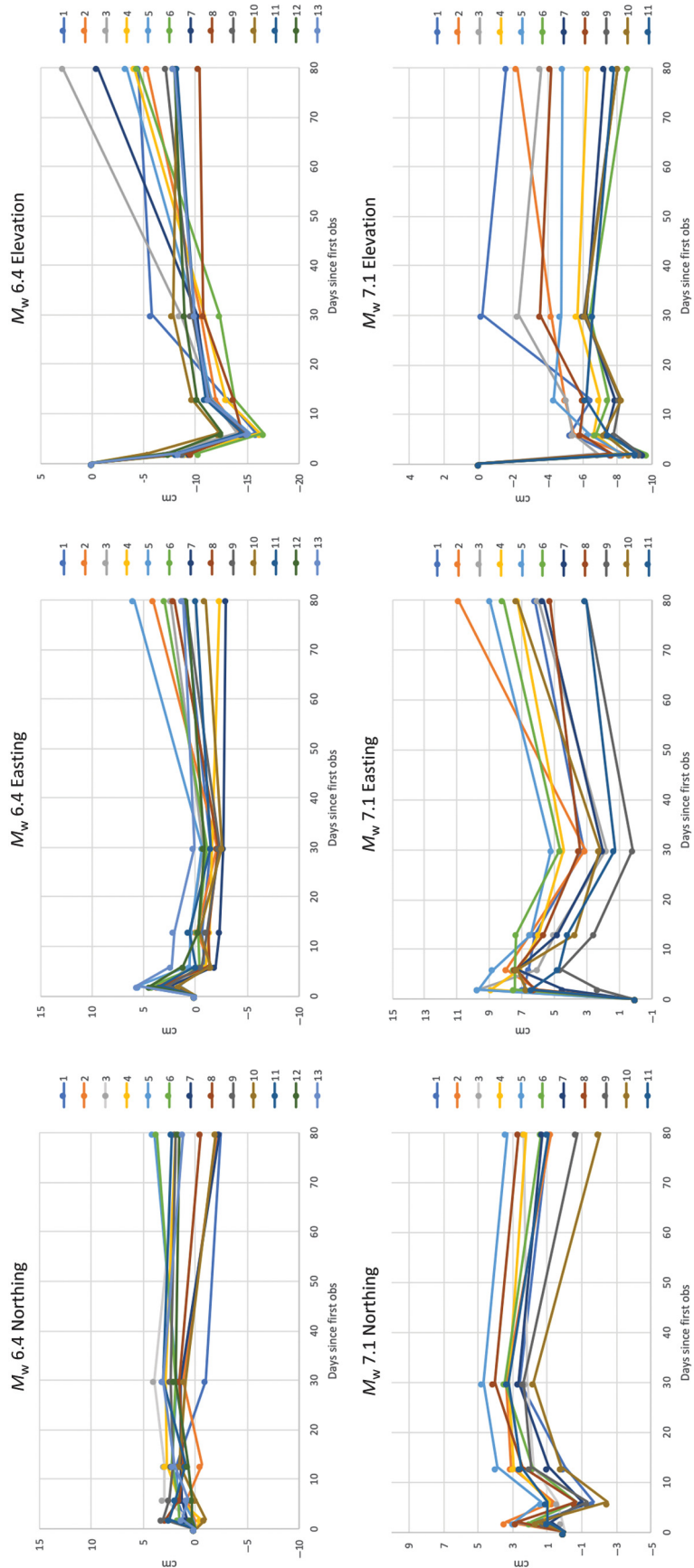


**Figure 7.** Plots of GCP positions for each earthquake show general postseismic trends. Locations of GCPs are identified in Figures 3 and 4. Values are relative to the first day of observing on 9 July 2019.

We plotted the north, east, and vertical positions of the GCPs, as they changed relative to the first day of observations (Fig. 7). Our results have greater motion than the millimeter of motion observed with nearby temporary continuous GPS stations placed along Highway 178 near our survey areas (Murray *et al.*, 2019). Postseismic InSAR images show up to decimeter level postseismic motions, which are more similar to our results (Fielding *et al.*, 2019). There appears to be an initial sense of motion that reverses within a week of the first survey. It is very possible that most of the changes from survey to survey are due to motion of the cloth targets, which were secured at the corners. By the end of the final survey on 27 September 2019, we had staked down all the GCPs in the center of the cross. Subsequent measurements might provide useful information on any ground surface motion overall and within the survey area. It is unclear if the elevation being different from the trend on the first day, 9 July 2019, is due to survey uncertainty or shows a reversal of vertical motion. Subsidence over two surveys at the  $M_w$  6.4 rupture suggests that the result may be accurate. Better comparison to the local continuous GPS surveys may shed light on this. If the GPS surveys are correct, then further motion on both faults may have caused subsidence from extension and normal faulting. A second mechanism such as poroelastic or viscoelastic rebound may be responsible for the reversal to uplift in the 7–10 days after the earthquake sequence. More likely, the overall repeatability for the surveys due to other factors such as human error or target motion is about  $\pm 5$  cm.

## Summary

sUAS observations of earthquake ruptures have proved useful for identifying surface cracking at the level of a few centimeters. sUAS observations complement and support field observations and can be used to identify additional fault splays or conjugate faulting that may be more difficult to find in the field. Continued observations will illuminate fine scale postseismic motions, which may be useful for separating postseismic mechanisms. Little postseismic deformation occurred on these two sections of the two ruptures in the first three months after the events, which is consistent with centimeter-level postseismic motion for the Landers and Hector Mine earthquakes.

## Data and Resources

Data products are available from GeoGateway at <http://geo-gateway.org> under the 3D imaging tab (Donnellan *et al.*, 2019). Raw images are available upon request. An app called Pix4DCapture is available at <https://www.pix4d.com/product/pix4dcapture>. Pix4Dmapper software package is available at <https://www.pix4d.com/product/pix4dmapper-photogrammetry-software>. All websites were last accessed in February 2020. The unpublished manuscript by C. A. Goulet, Y. Wang, X. Meng, T. Gallien, M. Winters, B. Tang, S. K. Ahdi, K. Hudnut, M. Hudson, S. Brandenburg, J. P. Stewart, K. Hudson, C. C. Nweke, P. Wang, A. Donnellan, and G. Lyzenga (2020), “Comparison of near-fault displacement interpretations from field

and aerial data for the M6.4 and 7.1 Ridgecrest earthquake sequence ruptures,” submitted to *Bull. Seismol. Soc. Am.*

## Acknowledgments

This work was carried out at the Jet Propulsion Laboratory (JPL), California Institute of Technology under contract with National Aeronautics and Space Administration (NASA). The work was supported by NASA’s Applied Science Disaster Response and Earth Surface and Interior programs. The authors thank Erik Conway, Chris Milliner, and Rob Zinke who assisted with the field observations. The authors also thank Naval Air Weapons Station (NAWS) China Lake, the Federal Aviation Administration, Edwards Air Force Base, NASA Armstrong Flight Research Center, and the JPL Safety Office for facilitation the small uninhabited aerial systems (sUAS) flights. C. Goulet’s was supported by the Southern California Earthquake Center (SCEC; Contribution Number 10036). SCEC is funded by National Science Foundation (NSF) Cooperative Agreement EAR-1600087 and U.S. Geological Survey (USGS) Cooperative Agreement G17AC00047, with additional support from the Pacific Gas and Electric Company.

## References

- Brandenberg, S. J., J. P. Stewart, P. Wang, C. C. Nweke, K. Hudson, C. A. Goulet, X. Meng, C. A. Davis, S. K. Ahdi, M. B. Hudson, *et al.* (2019). Ground deformation data from GEER investigations of Ridgecrest earthquake sequence, *Seismol. Res. Lett.* doi: [10.1785/0220190291](https://doi.org/10.1785/0220190291).
- Donnellan, A., G. Lyzenga, J. Wang, M. Pierce, and C. Goulet (2019). High-resolution targeted 3D imaging postseismic products of the Ridgecrest M6.4 and M7.1 earthquake sequence, *Dataset*, doi: [10.5967/5sq2-rs60](https://doi.org/10.5967/5sq2-rs60).
- Dreger, D., and A. Kaverina (2000). Seismic remote sensing for the earthquake source process and near-source strong shaking: A case study of the October 16, 1999 Hector Mine earthquake, *Geophys. Res. Lett.* **27**, no. 13, 1941–1944.
- Field, E. H., G. P. Biasi, P. Bird, T. E. Dawson, K. R. Felzer, D. D. Jackson, K. M. Johnson, T. H. Jordan, C. Madden, A. J. Michael, and K. R. Milner (2015). Long-term time-dependent probabilities for the third Uniform California Earthquake Rupture Forecast (UCERF3), *Bull. Seismol. Soc. Am.* **105**, no. 2A, 511–543.
- Fielding, E., M. Simons, O. Stephenson, M. Zhong, S. H. Yun, C. Liang, S. Sangha, Z. Ross, M. H. Huang, and B. Brooks (2019). Geodetic imaging of the coseismic and early postseismic deformation from the 2019  $M_w$  7.1 and  $M_w$  6.4 Ridgecrest earthquakes in California with SAR, *AGU 2019 Fall Meeting*, San Francisco, California, December 2019.
- Hauksson, E., L. M. Jones, K. Hutton, and D. Eberhart-Phillips (1993). The 1992 Landers earthquake sequence: Seismological observations, *J. Geophys. Res.* **98**, no. B11, 19,835–19,858.
- Jacobs, A., D. Sandwell, Y. Fialko, and L. Sichoix (2002). The 1999 ( $M_w$  7.1) Hector Mine, California, earthquake: Near-field postseismic deformation from ERS interferometry, *Bull. Seismol. Soc. Am.* **92**, no. 4, 1433–1442.
- Marr, D. (1980). Visual information processing: The structure and creation of visual representations, *Phil. Trans. Roy. Soc. Lond. B.* **290**, no. 1038, 199–218.

- Murray, M. H., C. Guillemot, A. Aspiotes, R. Turner, J. Parsi, B. A. Brooks, J. O. Langbein, and J. J. McGuire (2019). The USGS Southern California GNSS Network: Real-time estimates of crustal deformation associated with the 2019 Ridgecrest, California, earthquake sequence, *AGU Fall Meeting 2019*, San Francisco, California, December 2019.
- Owen, S., G. Anderson, D. C. Agnew, H. Johnson, K. Hurst, R. Reilinger, Z. K. Shen, J. Svarc, and T. Baker (2002). Early postseismic deformation from the 16 October 1999 Mw 7.1 Hector Mine, California, earthquake as measured by survey-mode GPS, *Bull. Seismol. Soc. Am.* **92**, no. 4, 1423–1432.
- Pickering, A., K. Thomas, D. J. Ponti, C. M. Rosa, J. L. Hernandez, and J. L. L. Blair (2019). Rapid synthesis of surface rupture mapping and observation data during response to the 2019 Ridgecrest earthquake sequence, CA, *AGU Fall Meeting 2019*, AGU, San Francisco, California, December 2019.
- Ponti, D. J., J. L. Blair, C. M. Rosa, K. Thomas, A. J. Pickering, S. Akciz, S. Angster, J.-P. Avouac, J. Bachhuber, S. Bacon *et al.* (2020). Documentation of surface fault rupture and ground deformation features produced by the Ridgecrest M6.4 and M7.1 earthquake sequence of July 4 and 5, 2019, *Seismol. Res. Lett.*
- Scholz, C. H. (1972). Crustal movements in tectonic areas, *Tectonophysics* **14**, nos. 3/4, 201–217.
- Shen, Z. K., D. D. Jackson, Y. Feng, M. Cline, M. Kim, P. Fang, and Y. Bock (1994). Postseismic deformation following the Landers earthquake, California, 28 June 1992, *Bull. Seismol. Soc. Am.* **84**, no. 3, 780–791.
- Sylvester, A. G. (1993). Investigation of near-field postseismic slip following the Mw 7.3 Landers earthquake sequence of 28 June 1992, California, *Geophys. Res. Lett.* **20**, no. 11, 1079–1082.
- Ullman, S. (1979). The interpretation of structure from motion, *Proc. Math. Phys. Sci.* **203**, no. 1153, 405–426.
- Wallach, H., and D. N. O'Connell (1953). The kinetic depth effect, *J. Exp. Psychol.* **45**, 205–217.

---

Manuscript received 25 September 2019

Published online 18 March 2020